Mechanical Activation Effect
on Self-Sustaining Combustion Reaction in Mo−Si System

CH. GRAS[1,2], D. VREL[3], E. GAFFET[1] and F. BERNARD[2]

[1]*"Nanomaterials : Far from Equilibrium Phase Transition" group UMR 5060 CNRS - UTBM F-90010, Belfort (France)*

E-mail: Gaffet@utbm.fr

[2]*"Fine Grained Materials" group LRRS UMR 5613 CNRS/Universite de Bourgogne BP 47 870 21078 DIJON Cedex (France)*

E-mail: fbernard@u-bourgogne.fr

[3]*LIMHP CNRS Av. J. B. Clement F-93430 Villetaneuse (France)*

E-mail: vrel@limph.univ-paris13.fr

Abstract

Nanostructured molybdenum disilicide ($MoSi_2$) compound was synthesized using an alternative route called MASHS (Mechanically Activated Self-propagating High-temperature Synthesis). This original process combines a short-duration ball milling with a self-sustaining combustion. These two steps were investigated in this paper. The microstructure evolution of powder mixture during mechanical activation was monitored using XRD profiles analysis and TEM investigations. Short-duration ball milling of (Mo + 2Si) powders results in Mo and Si nanocrystallites in micrometric particles. It was demonstrated that a pure α-$MoSi_2$ with nanometric structure ($D_{MoSi_2} = 88$ nm) could be produced *via* a very fast combustion front in contrast with the classical SHS process.

INTRODUCTION

Due to the attractive high-temperature properties, silicides of various metals have been the focus of numerous investigations [1−4]. In the case of the molybdenum disilicide ($MoSi_2$), the combination of low density ($d = 6.23$), high-melting point (2293 K) and very good resistance to high temperature corrosion allows considering this silicide for use within temperature range as high as 1523 K for turbine engine applications. At this temperature, the strength and the oxidation resistance of this refractory silicide phase are better than those of most metallic and ceramic-based composite materials [2]. Molybdenum disilicide ($MoSi_2$) is a dimorphous phase [5]: the tetragonal C11b type α-$MoSi_2$ phase is stable up to 2173 K; above this temperature α-$MoSi_2$ is transformed to hexagonal C40 type β-$MoSi_2$ phase. This high-temperature phase (β-$MoSi_2$) melts in a congruent form at 2293 K.

$MoSi_2$ was synthesized by various methods such as conventional arc-melting and casting, powder pressing-sintering (typically 1473 K for 2 h as reported by Zhang and Munir [6]) and reaction synthesis hot pressing. These methods should overcome two main difficulties: the high melting point of the refractory silicide and the possibility of oxygen incorporation during these particular syntheses. An alternative method was proposed by Le Caër *et al.* [7] who reported on the production of $MoSi_2$ by mechanical alloying using a vibrating system. They were followed by Schwartz *et al.* [8], Patankar *et al.* [9], and Yen *et al.* [10] using different apparatus for the same purpose. Some authors [9, 10] deal with particular explosive phase formation during milling of a stoichiometric Mo/2Si mixture of elemental powders.

A well-known route to produce massive molybdenum silicide consists in using the high exothermicity of its formation reaction (ΔH_f^o ($MoSi_2$) = -111 kJ/mol). The technique has received wide attention and is known as Self-propagating High-temperature Synthesis (SHS) or combustion synthesis. In this technique, a sample is made by cold compaction of

stoichiometric elemental powder mixture. The green product is heated on one side, a reaction is first initiated in a small volume and then gradually spreads through the sample. When the reaction is initiated, combustion front transverses the whole sample and leads directly to the formation of the material. In the SHS process, the time required for the synthesis is much shorter than for the other powder metallurgy techniques [11−13] and the temperature elevation is faster ($\gg 10^3$ K/s) than the conventional method.

Numerous factors are important for the successful initiation of combustion front. Generally, porosity, heating rate, the grain size or the stoichiometry of the primary mixture play an important role. The combustion wave can be defined by: the rate ot propagation (U) through the sample, ignition temperature (T_{ig}), heating rate (E_{ch}) in the front and combustion temperature (T_c) which is the maximum temperature reached during the SHS process [14].

An alternative method to synthesize molybdenum disilicide, named Mechanically Activated Annealing Processing (M2AP), was proposed by Gaffet *et al.* [15, 16]. Such a solid state processing combines a short-duration high-energy ball milling and low temperature isothermal annealing. Gaffet *et al.* [15] reported on the possibility to obtain pure nanocrystalline $MoSi_2$ compounds after 2 h of mechanical treatment followed by annealing for 2 h at 1073 K. Recently, a new version of the SHS process was proposed by Bernard and Gaffet [17]. The so-called MASHS consists of a short-duration high-energy ball milling step [18, 19l] followed by self-sustaining reaction. This process was successfully applied to produce nanocrystalline (30−35 nm) bulk FeAl intermetallic compacts with relative density close to 80 % [20−22].

This paper presents the results on the MASHS process which is applied to produce molybdenum disilicide compacts. Based on X-ray diffraction pattern characterizations, scanning electron microscopy observations, specific surface measurements and chemical analysis, the elemental nanocrystalline mixture obtained after the mechanical activation step and the nanocrystalline intermetallic phases produced by MASHS process were investigated.

EXPERIMENTAL PROCEDURE

Mechanical activation

Pure elemental powders (Mo + 2Si) were co-milled inside a planetary mill hereafter called the G5 machine [23]. The powders were sealed into stainless steel vials with a volume of 125 ml with five stainless steel balls (15 mm in diameter, 14 g in mass). The vials are fixed onto a rotating disc (rotation speed Ω) and rotate in the opposite direction to the disc with a speed ω. The duration of the milling process is denoted Δt. In summary, each milling condition is characterized by three important parameters ($\Omega/\omega/\Delta t$). Table 1 shows the shock energy, frequency and shock power used to activate 10 g of stoichiometric Mo + 2Si elemental powder mixture for each ball milling condition. These figures are based on the kinematic studies of the G5 milling machine by Abdellaoui and Gaffet [23, 24].

Based on primarily studies of M2AP process in Fe−Si [25] and Mo−Si [15] systems, different shock powers and milling durations were chosen to investigate the effect of ball milling on the Mo + 2Si powders reactivity in SHS conditions. In addition to the milled powders, a reference mixture of stoichiometric elemental powders shaken during 3 h in a Turbula apparatus was prepared.

Cold compaction process

As-milled powders were pressed into cylindrical vials using a uniaxial load of 300 MPa for 60 s. After compaction, samples were brittle and measured 8 mm in diameter (ϕ) and 8 to 10 mm in height (h). Geometrical porosity of the green product was determined using size and mass measurements.

TABLE 1

Ball milling conditions and calculated characteristics determined from ref. [24]

Ω/ω, rpm	Δt, h	Shock energy, J	Shock frequency, Hz	Shock power, W
250/250	1−3−4−6	0.08−0.09	28.5	2.2
350/250	1−3	0.16−0.17	33	4.8

Structural investigation

X-ray diffraction (XRD) meatsurements were performed with a SIEMENS D 5000 high-resolution powder diffractometer. Mono-chromatic CuK_β X-rays ($\lambda = 0.1392$ nm) were obtained with a secondary focusing graphite monochromator and used for profile line analysis. Routine X-ray phase identification was carried out with CuK_α wavelength (0.154 nm). Pattern decomposition was carried out by means of profile-fitting program PROFILE* to obtain parameters defining the position, height, area, integral breadth and shape of individual Bragg reflections. XRD composition was performed using peak intensity measurement (I_X followed by the calculation of the ratio $R = I_X/\Sigma I_X$ where I_X is the XRD intensity for main peak of compound X.

TEM observations were performed on powder dispersed in alcohol onto grid after a short ultrasonic treatment. This work was done in collaboration with M. F. Beaufort from LPM University of Poitiers (France).

Chemical analysis and specific surface measurements

Chemical analysis was performed to determine the composition of the milled powders and to estimate the contamination from abrasion of the milling tools. These experiments were conducted on a JEOL 6400 F scanning electron microscope fitted with ELX LINK Oxford energy dispersive X-ray analyzer (EDX). ZAF-4 quantitative correction software was used to determine the atomic percentage of each element present in the mechanically activated powders.

In addition, the specific surface was measured using the Brunauer–Emmett–Teller (BET) method [26] based on N_2 adsorption. Particle size distribution was calculated from experiments carried out on a laser granulometer Coulter LS 130.

Ignition process

The SHS reaction was performed using a reaction chamber developed by J. C. Gachon *et al.* [27] in inert gas atmosphere to avoid material

---

* Available in the Socabin PC Software package DIFFRACT-AT supplied by Siemens.

oxidation. After 30 min of pumping, a stable flow of helium is generated through the 1 l volume of the combustion chamber. A specific Milar window allows observing the thermal evolution of the sample using an infrared camera. An electrical heater attached to the alumina sample holder allows preheating the sample to 523 K. The local pulse of thermal energy is supplied by a graphite resistor. The preheating step was performed to ameliorate ignition condition and to allow outgasing before the combustion.

Thermal analysis

Thermal data were recorded by an infrared imaging camera (model AVIO HGH TVS 2000 ST). Thermal infrared images were continuously recorded and directly transformed into digital data. Infrared thermography allows measuring the temperature evolution of whole sample surface with a temporal resolution close to 0.066 s. No direct interferences induced by the thermocouples embedded inside the sample are possible. Thermal mapping of the sample during the propagation of the combustion front can be established and informations such as thermal homogeneity or characteristics of steady state front propagation can be calculated.

The spatial resolution of the infrared detection system is 0.8 1.45 mm^2 per pixel. Infrared emissivity measurements were carried out on reacted and non-reacted samples at 393 K in IUSTI [28]. The value of the emissivity for Mo–Si system before and after reaction was found to be 0.8 and 0.9 and does not exhibit large variations between the initial and the final step. Instrumental corrections and calibration were carried out between 298 and 773 K on reacted sample in order to adjust infrared temperature determination.

MECHANICAL ACTIVATION STEP

Characterization of as-milled powders

Chemical analysis and specific surface measurements. The powder composition after the mechanical activation process was determined by EDX elemental chemical analysis on pressed

pellets. The contamination from the vials or stainless steel balls never exceeds at 1 % at. (main pollutant is Fe for the longest and most powerful ball milling conditions).

Specific surfaces (S_g) measured did not show any relevant evolution with the ball milling parameters (*i.e.*: Ω, ω and Δt). Nevertheless, S_g for all the mechanical activation conditions is 8 times higher than the value measured in the case of Turbula mixture (0.5 m^2/g). The particle size distribution is very broad (0.2 to 200 μm), and laser granulometry indicates that larger

grains are formed when milling duration is increased. Coupled to Secondary Electron Microscopy observations, this result shows that ball milling induces the formation of aggregates by fracture-welding processes during severe mechanical treatment [28].

Phases analysis. As shown by Table 2, mechanically activated powders are composed of Mo and Si elements except for the G5(350/250/3 h) and G5(250/250/4−6 h) milling conditions. Figure 1 shows three revealing examples of XRD patterns for three different
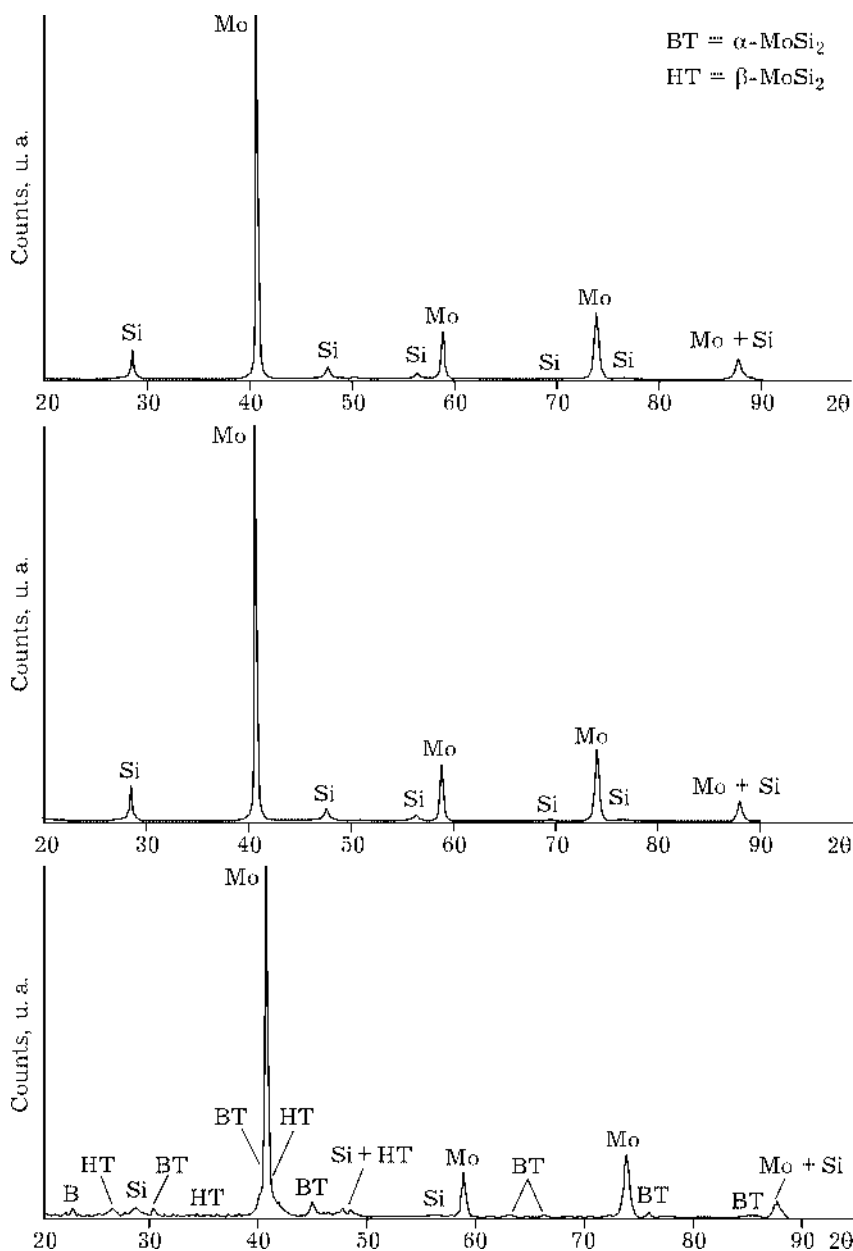

Fig. 1. Selected difractograms of as-milled powders (λ = 0.154 nm): *a* − G5(250/250/3 h), *b* − G5(350/250/1 h), and *c* − G5(350/250/3 h).

TABLE 2

As-milled powders characterization: XRD phases

Ball milling conditions	XRD phases
Tubula M, 3h	Mo*, Si
250/250/1 h	Mo*, Si
250/250/3 h	Mo*, Si
250/250/4 h	Mo*, Si (α- and β-MoSi$_2$)
250/250/6 h	Mo*, Si (α- and β-MoSi$_2$)
350/250/1 h	Mo*, Si
350/250/3 h	Mo*, Si (α- and β-MoSi$_2$)

* $0.8 > R > 0.6$, where $R = I_X/\Sigma I_X$.

ball milling conditions. The proportion of α– and β-MoSi$_2$ phases induced by the direct mechanical alloying process is low but can reach 8 % mass in the case of G5(350/250/3 h) powder. The stabilization of the β-MoSi$_2$ compound at room temperature is reported by several authors [8, 30, 31]. L. Liu *et al.* [32] impute this behavior to the kinetic competition on account of hexagonal phase during ball milling.

A very fast decrease in the intensity of the Si X-ray diffraction line was observed for the shortest ball-milling duration. Based on former works [15], a decrease in the Si diffraction peak intensities during ball milling can be explained by amorphization process and the formation of new phases (α- and β-MoSi$_2$) induced by direct mechanical alloying.

Mo cell parameter does not exhibit large evolution during ball milling ($a = 0.3147 \pm 0.0003$ nm). No evidence of solid solution Mo(Si) was found during short-duration ball milling. In the case of Si, the weak intensities of the three main peaks make the cell parameter determination a bit tricky.

Determination of crystallite size and microstrains from XRD profile line analysis. X-ray diffraction line broadening is influenced by the microstructure of the solid and is a valuable technique for unique characterization of a material in terms of size and morphology of crystallites (a region over which diffraction is coherent) and imperfections (microstrains, *d*-spacing fluctuations, stacking faults, *etc.*). To obtain these parameters defining the integral breadth and the shape of the individual Bragg reflections, pattern decomposition was carried

out by means of the profile fitting program PROFILE. A correction for the instrumental broadening was applied using the Wagner method [33]. The line profiles were modeled by symmetric pseudo-Voigt functions considered as a linear combination of Lorentzian − Gaussian functions (*i.e.*: $P − V = \eta L + (1 − \eta)G$).

For most of these profiles, the mixing factor (η) was close to 1 (or slightly larger), indicating that the profile shape was mainly Lorentzian (or even super-Lorentzian). The super-Lorentzian profile shape was observed in several compounds such as nickel oxide [34], zinc oxide, and BaF$_2$ [35]. It seems that this particular profile shape is due to the presence of an important amount of crystallites having a very small size (<10 nm) [35]. Clearly, it is an example for which the Voigt approach cannot be applied. Therefore, Williamson−Hall [36] plots ($\beta^* = \beta\cos\theta/\lambda$ *vs.* $d^* = 2\sin\theta/\lambda$) were used to determine the mean apparent crystallite size and the microstrains respectively given by the y intercept and the slope of the straight line. A typical example of Williamson−Hall plots for Mo and Si in the case of the G5(250/250/3 h) ball milling condition is presented in Fig. 2.
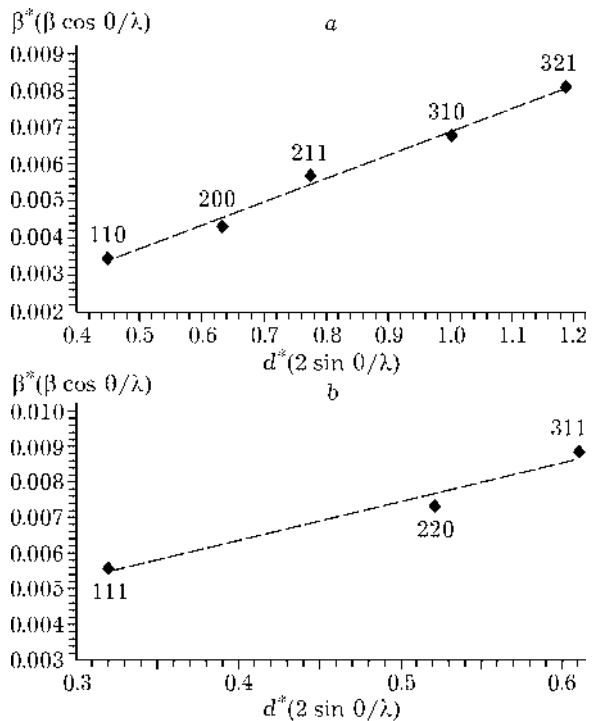

Fig. 2. Williamson−Hall plots for Mo (*a*) and Si (*b*) powders obtained in the case of the G5(250/250/3 h) ball milling conditions.

The Williamson−Hall plots for Mo and Si give the following informations:

(i) In the case of molybdenum, the integral breadth of all reflections linearly increases with $d*$ with a positive slope and there was a non-zero intercept. This suggests the existence of a shape and size isotropy for Mo crystallites. In Table 3, the apparent size of Mo crystallites (hereafter called ε_{Mo}) and the lattice strains (hereafter called η_{Mo}) are given with the linear regression coefficient for all [hkl] reflections (R^2_{Mo}) obtained during analysis of Williamson−Hall plots. This table shows that the Mo crystallite size decreases with ball milling duration and with increasing injected mechanical power. Indeed, the Mo crystallites become nanosized (50−55 nm) after a ball milling duration of 3 h for mechanical injected power equal to 2.2 or 4.8 W. The small evolution of R^2_{Mo} indicates that the «pseudo-spherical shape» of Mo crystallites seems to be maintained during the high-energy ball milling step.

(ii) For silicon, the integral breadths of all the reflections increase linearly with $d*$ with a positive slope and non-zero intercept. This suggests the existence of microstrains and

TABLE 3

Evolution of crystallite size ε_X, microstrains η_X and R_X (linear regression coefficient) obtained from Williamson−Hall plots for each ball milling condition (X = Mo or Si)

Ball milling conditions	ε_{Mo}, nm	η_{Mo}, $\times 10^3$	R^2_{Mo}	ε_{Si}, nm	η_{Si}, $\times 10^3$	R^2_{Si}
Tubula M, 3h	>500	−	−	>500	−	−
250/250/1 h	105	2.0	0.89	63	1.8	0.60
250/250/3 h	50	1.4	0.70	28	1.9	0.92
250/250/4 h	40	1.3	0.82	(18)	2.4	0.20
250/250/6 h	47	1.6	0.87	(68)	0.9	0.04
350/250/1 h	292	2.6	0.90	52	4.1	0.91
350/250/3 h	54	1.7	0.87	34	3.4	0.88

isotropic crystallite sizes too. Nevertheless, from the G5(250/250/4 h) ball milling condition, the XRD peak shape becomes slightly super-Lorentzian. This shape could be due to the presence of very small particles and amorphous phases. Table 3 represents the evolution of crystallite size (ε_{Si}), the microstrains (η_{Si}) and R^2_{Si} (linear regression coefficient) obtained from Williamson−Hall plots *vs.* the ball milling conditions. In Table 3, a R^2_{Si} coefficient equal to 0.92 reveals an isotropic behaviour of Si

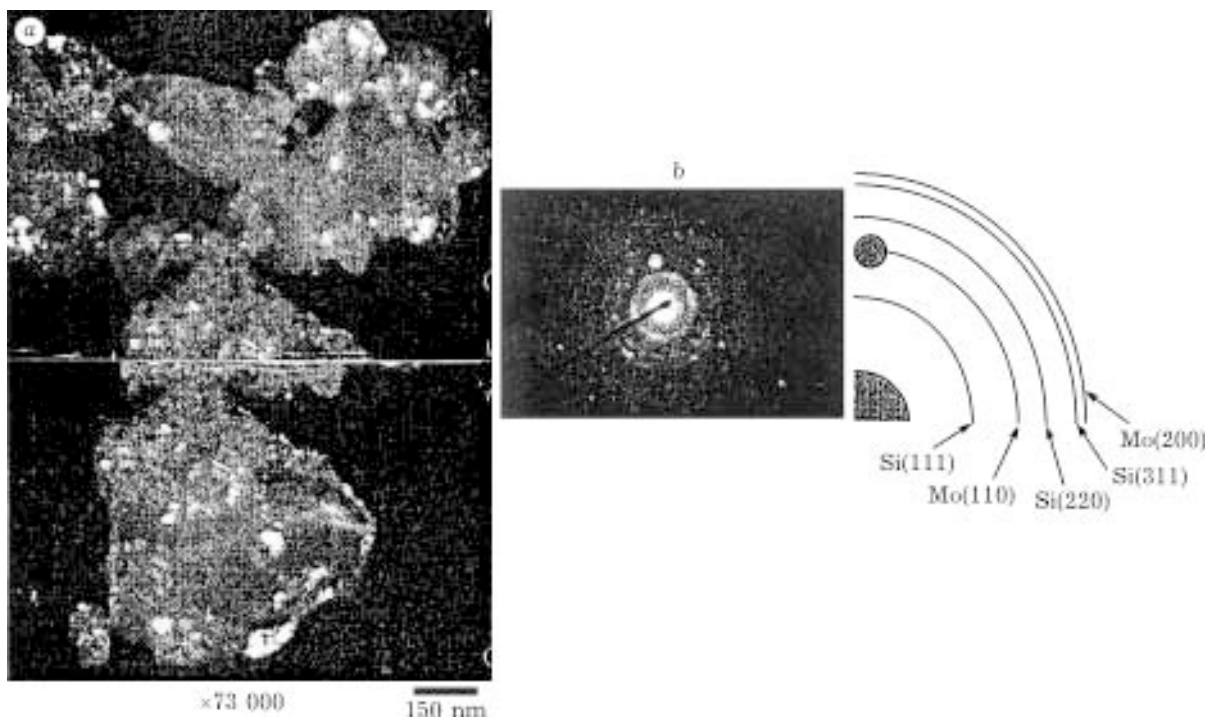Fig. 3. TEM observation of as-milled powders particles from G5(350/250/3 h) condition: *a* − Mo(110) dark-field micrograph, *b* − associated SAD.

powders for the short ball milling duration ($\Delta t < 3$ h) but thus the linear regression coefficient falls down very quickly (0.20–0.04) from G5(250/250/4 h) ball milling condition. Indeed, the brittle behavior of silicon is responsible for the amorphous phase formation and very fast decrease of Si crystallites size.

Consequently, mechanical activation leads to a rapid decrease in silicon crystallite size. During the first hour of ball milling a mixture composed of nanosized Si crystallites and submicronic molybdenum crystallites is formed. The effective decrease in ϕ_{Mo} is obtained after 3 h of low intensity ball milling. If the injected power increases, the necessary time drops to 1 h.

In summary, based on SEM, BET and XRD investigations, the structure of as-milled powders may be considered as aggregates (0.2 to 200 μm) composed of nanometric crystallites of molybdenum and silicon. In order to confirm this hypothesis, some TEM observations were carried out on as-milled powder aggregates. Figure 3, *a* shows Mo dark-filed electron micrograph of agglomerate in the case the powder G5(350/250/3 h). The light regions correspond to Mo particles (size ranging from 5 to 100 nm) spread about the large powder grains (diameters 0.6 to 0.8 μm). The possibility that some α-MoSi$_2$ discrete rings could overlap the Mo(110) one cannot be excluded. Nevertheless, the low proportion of α-MoSi$_2$ can participate in the formation of bright zones but the main origin is assumed to be the presence of Mo crystallites. TEM observations coupled to XRD

profile line analysis allow to precise the particular structure formed during mechanical activation: the as-milled powders are composed of large (0.2–200 μm) nanostructured aggregates of Mo and Si crystallites.

SELF-PROPAGATING HIGH-TEMPERATURE SYNTHESIS STEP: INFRARED MEASUREMENTS

From infrared image analysis, thermal profile during combustion reaction in the case of the mechanically activated (G5(350/250/1 h)) and the classical SHS process can be determined for several points on the sample surface (Fig. 4). For each process, two infrared thermograms recorded during the combustion front for two consecutive selected areas (x_1 and x_2) are plotted in Fig. 3, *a*. The temporal evolution of temperature is typical of SHS process. Using a fast preheating step ($T_0 = 523$ K), the maximal combustion temperature reached during the two processes is close to 2100 K. The combustion temperature (T_c) is higher than that reported in the literature. The main explication is the effect of the additional heat produced by preheating. If the adiabatic calculation is considered, the adiabatic temperature for $T_0 = 523$ K is equal to 2112 K which is comparable to T_c recorded by IR thermography.

The propagation rate was determined from the delay for the wave to reach a defined position x. The average value during the whole process (see Fig. 3, *b*) was found to be equal to
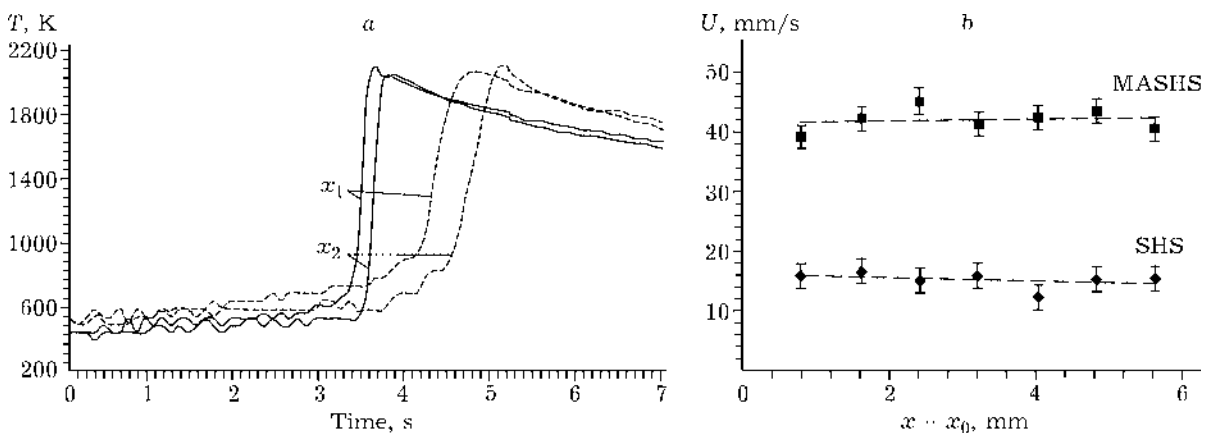

Fig. 4. IR analysis: *a* – infrared thermograms for two different points (x_1 and x_2) on the samples: comparison of MASHS (*continuous lines*) and classical combustion process (*dashed lines*); *b* – evolution of the combustion front velocity (U) during the propagation.

TABLE 4

Results of thermal analysis for different ball milling conditions

Ball milling conditions	T_c, K	U, mm/s	E_{ch}, °C/s
Turbula	1973 ± 20	14.0 ± 0.7	1850 ± 20
250/250/3 h	2120 ± 22	42.0 ± 2.1	7080 ± 49
350/250/1 h	2055 ± 21	42.5 ± 2.2	6600 ± 42
250/250/3 h	1810 ± 19	33.4 ± 1.7	2410 ± 19

Note. T_c is maximal combustion temperature; U is combustion front velocity; E_{ch} is maximal heating rate inside the combustion front.

TABLE 5

Porosity determination and XRD phase analysis of α-MoSi$_2$ produced by MASHS

Ball milling conditions	Porosity 1, % (before SHS reaction)	Porosity 2, % (after SHS reaction)	Phases after reaction XRD
250/250/1 h	41.9	48.9	α-MoSi$_2$*, (Mo)
350/250/3 h	41.8	49.6	α-MoSi$_2$*, (Mo), (M5)
250/250/4 h	41.8	42.4	α-MoSi$_2$*, (Mo), (M5)
250/250/6 h	40.2	n/d	α-MoSi$_2$*
350/250/1 h	42.2	52.3	α-MoSi$_2$*
350/250/3 h	36	44	α-MoSi$_2$*

Note. Porosity 1 is mass and geometric volume measurement; porosity 2 is He picnimetrie and hydrostatic pressure of Hg.

* $1 > R > 0.8$, where $R = I_X/\Sigma I_X$, I_X is the XRD intensity for major peak of compound X.

14 mm/s for classical SHS and 42 mm/s for G5(350/250/l h) ball milling condition, respectively. The combustion wave exhibits a steady state along the sample. Table 4 sums up thermal results such as the maximum combustion temperature (T_c), the combustion front velocity (U) and the maximum thermal heating rate (E_{ch}) measured during the combustion process. In general, MASHS combustion front is faster than the SHS one and, except 05(350/250/3 h), the maximum thermal heating rate increases when mechanical activated powders are used as raw materials.

MASHS END PRODUCT CHARACTERIZATIONS

Evolution of porosity during MASHS process

The porosity of products before (porosity 1) and after (porosity 2) combustion is presented in Table 5. After SHS reaction, volume measurement by helium picnometry and by hydrostatic Hg pressure method were carried out to determine the open porosity in MASHS materials (denoted porosity 2 in Table 5). For each sample, the end product porosity is larger than the green product porosity (average increase 15−20 %). SEM observations and Hg intrusion porosimetry indicate that pore diameter was mainly ranging from 1 to 10 μm.

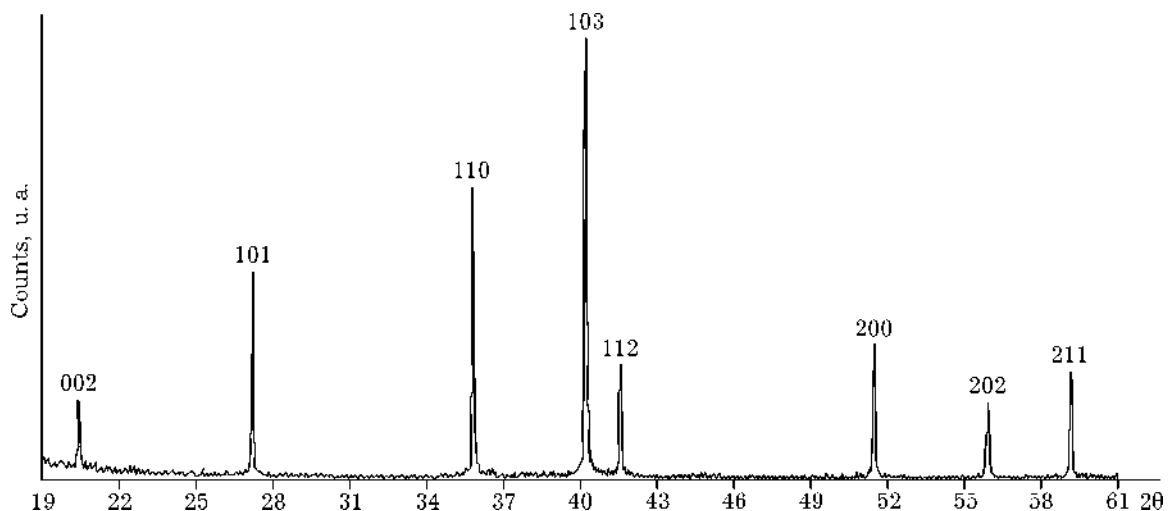This evolution is in agreement with Z. A. Munir's works [37] and can be attributed

Fig. 5. End products identification: XRD analysis CuK$_\beta$ = 0.139 nm) for the G5(350/250/3 h) ball milling condition.

to the volatilization of impurities due to the high temperature reached during combustion and the molar volume decrease [38] due to the formation of $MoSi_2$ from $Mo + 2Si$ ($\Delta V = -40.6$ %).

XRD end products characterizations

Each sample made from different mechanically activated powders was reacted following the SHS process. XRD diffractograms after reaction ball milling conditions show that the final product contains 95 to 100 % of $MoSi_2$ low-temperature compound. One example is given in Fig. 5.

As reported in Table 5, some ball milling conditions lead to the formation of Mo-rich phases such as Mo_5Si_3 (denoted M5 in Table 5) or Mo. MASHS sample G5(350/250/3 h) contains no XRD detectable trace of high-temperature β-$MoSi_2$ phase after combustion reaction. This metastable phase induced by direct mechanical alloying was transformed into the low-temperature form due to high temperature reached in the combustion front. This transformation is the consequence of structural rearrangement ABCABC to ABAB which can exist under extreme thermal conditions [39].

Microstructural investigation of α-MoSi₂ produced by MASHS route

In order to determine the α-$MoSi_2$ fine microstructure, XRD profile investigations were carried out on samples obtained after MASHS proc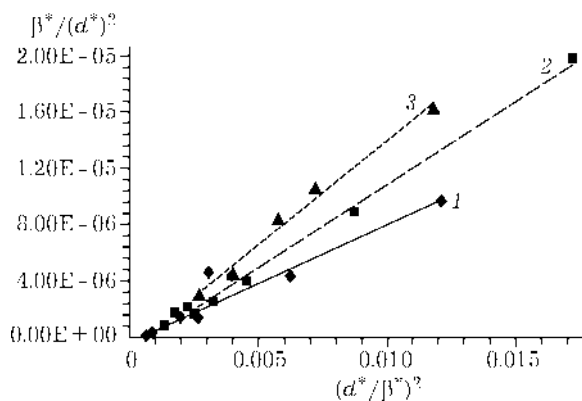ess. Line profiles were modeled by sym-metric pseudo-Voigt functions and correction for instrumental broadening was carried out by Wagner method [33]. On account of pseudo-Voigt profiles, the Voigt approach and the Halder−Wagner method [36] can be applied to eight diffraction peaks of α-$MoSi_2$. From Halder−Wagner plot, ($\beta^*/(d^*)^2$ vs. $(d^*/\beta^*)^2$, the slope gives the mean apparent crystallite size; the y intercept of the straight line yields the microstrains. Two examples of typical Halder−Wagner plots are presented for $Mo + 2Si$ G5(350/250/1 h) and G5(350/250/3 h) ball milling conditions in Fig. 6. In addition, the Halder−Wagner plot for the Turbula mixture (classical SHS) is shown as a reference to compare end product microstructures.

As shown by the Halder−Wagner plots for the three samples, $\beta^*/(d^*)^2$ linearly increases with $(d^*/\beta^*)^2$ for all reflections. Consequently, the α-$MoSi_2$ crystallites exhibit spherical shape and isotropic behavior in terms of both size and microdistorsions. From a least squares fit, the slope of the straight line gives the mean apparent crystallite size (ϕ_{MoSi_2}) equal to 66 nm for G5(350/250/3 h), 85 nm for G5(350/250/3 h) and 160 nm for classical SHS. The y intercept is slightly negative but very close to 0. Consequently, the microstrains are not measurable by the XRD profile line analysis method. This result indicates that the product could be considered as microstrain free whatever the (hkl) directions studied.

These results indicate that the molybdenum disilicide crystallite can be described using a spherical mode [36]. The diameter (D_{MoSi_2}) of this sphere can be deduced from the apparent size using the relation $D_{MoSi_2} = 4\varepsilon_{MoSi_2}/3$ [36]. For G5(350/250/3 h) condition, the crystallite diameter is equal to 88 nm whereas for the Turbula mixture the calculated D_{MoSi_2} is equal to 214 nm.

DISCUSSION

Mechanically activated $Mo + 2Si$ powders were found to be composed of nanostructured powder particles without large evolution of chemical composition. Therefore, the intermixing of reactive components is obtained at a nanometric scale. Mechanical activation, defined as a short-duration ball milling, forms

Fig. 6. Halder−Wagner plots for α-$MoSi_2$ obtained from classical Turbula M for 3 h (1), G5(350/250/1 h) (2), and G5(350/250/3 h) (3) ball milling conditions.

numerous 3D polyinterfaces of good quality between Mo and Si. In fact, fracture-welding process [39, 40] during mechanical activation is able to increase the contact surface area between reactants and destroy the oxide layer generally observed on commercial raw materials.

The quality of ball milling is important to obtain pure molybdenum disilicide. In fact, a short and less powerful mechanical treatment {*i.e.* G5(250/250/1 h)} induces the presence of Mo non-reacted particles due to the heterogeneity of the mixture and/or the large Mo particle size. For longer mechanical activation duration (*i.e.* 3 h), a small depletion in Si compound in ball milled powder composition can explain the formation of Mo and Mo-rich phases (Mo_5Si_3 in Mo–Si phases diagram [5]) during MASHS process. This behavior was observed by Malhouroux–Gaffet *et al.* [15] during their studies of the M2A process in the Mo–Si system.

Each mechanical activation condition leads to the formation of a fast combustion wave. As shown in Table 4, the combustion front velocity is multiplied by 3 from the reference value (Turbula mixture). The same trends were reported by F. Chariot *et al.* [17, 20] concerning the MASHS synthesis of intermetallic FeAl, by H. P. Li *et al.* for complex combustion reactions between TiO_2, Al and B_2O_3 [41] or by J. Lagerborn *et al.* [42] for the production of Ni_3Si by SHS of ball milled elemental powders.

Therefore, the mechanical activation process, by improving the number of contacts between reactants, increases the velocity of combustion wave. One interesting parallel could be done with SHS reaction initiated in multilayer systems such as Ni/Al [43] or Nb/Si [44] (thickness <250 nm). According to the authors, the combustion front velocity increases when the layers become finer. In a classical mix (*i.e.* Turbula mix, ultrasonic dispersion and so on), the contacts between reactants can be modeled as two spheres contacting in one point. On the contrary, the mechanical activation process increases the contact area between Mo and Si crystallites inside a powder particle. The combustion reaction takes place inside the grains of the powder rather than between micrometric particles.

Based on time-resolved X-ray diffraction observations [45, 46] and literature review [47–49], the unique reaction involving in the formation of $MoSi_2$ is heterogeneous: $Mo(s) + 2Si(l) \rightarrow MoSi_2(s)$. The process follows the equilibrium model of Khaikin–Merzhanov–Aldushin [50] when liquid silicon reacts with solid molybdenum into the combustion front. In this model, chemical reaction controls the combustion propagation and, consequently, affects the front velocity. A decrease in crystallite size and an increase in the contact surface between reactants promote the reaction and «energize» the chemical evolution.

The thermal energy is liberated more rapidly as shown by the difference in maximum thermal heating (E_{ch}) between MA and non-MA SHS. This observation is confirmed by the works of P. Zhu *et al.* [51] on Ni/Al multilayered nickel and aluminium foils. In addition, F. Bordeaux *et al.* [52] indicate that the heat production can be promoted when multilayer structure of reactants is fine. Consequently, mechanical activation modifies the kinetic of the reaction, affects the heat generation but does not change the maximal temperature reached during the combustion (T_c). In the case of G5(250/250/3 h or 350/250/1 h) conditions, a slight decrease in T_c from theoretical values calculated for adiabatic conditions (T_{ad}) is due to the heat losses during the combustion [53].

To the contrary, for the G5(350/250/3 h) condition, a small amount of α-$MoSi_2$ and β-$MoSi_2$ in the as-milled powder reduce the propagation front velocity, the maximal combustion temperature and the maximal heating rate during the process. Thermal balance is affected by the presence of α-$MoSi_2$ and β-$MoSi_2$ compounds [54] because they act like thermal well or «diluent» [55].

The XRD microstructural investigations lead to conclude that MASHS process is a suitable technique to produce nanometric α-$MoSi_2$ material; nevertheless, the product has low density (52 % of the theoretical one).

As shown in Fig. 6, an increase in the time of mechanical activation leads to the productions of finer α-$MoSi_2$ crystallites. The same trend is observed when the shock energy which is proportional to Ω^2) is intensified. The short-duration ball milling seems to play an important role in controlling the final microstructure of molybdenum disilicide. According

to the literature, two hypotheses can be enounced to describe the α-MoSi$_2$ formation: the first one involves the formation of MoSi$_2$ from the interface between solid Mo and liquid Si [48] and the other one can be expressed as dissolution of molybdenum in liquid silicon followed by nucleation of α-MoSi$_2$ from the supersaturated liquid Si(Mo) [49]. Increasing the surface of Mo/Si interfaces would increase the number of reaction sites in the first scenario. In the second hypothesis, nucleation and growth of α-MoSi$_2$ will be the two determining steps of the process. Mechanical activation would promote the number of potential nucleation sites and produce finer crystallites. This conclusion is based on simulations describing the reaction Nb(l) +C(s) $\to$ NbC(s) made by Y. Zhang *et al.* [55]. They reported that a large number of potential nuclei could decrease the grain size and accelerate the combustion wave. In addition, the presence of mechanically alloyed MoSi$_2$ (MA MoSi$_2$) can have a positive effect on final microstructure because MA MoSi$_2$ acts as heterogeneous nucleation sites with a good distribution inside the grains and decrease the combustion temperature. Consequently, the crystallite growth is limited by lower temperature and large number of grains which are formed at the same time. This last remark added to the small size of Mo crystallites could be the reason of the nanostructure production after MASHS.

The role of mechanical activation was presented as the result of interactions with the chemical reaction, but heat conductivity (K) is also an important parameter. In the case of an optimum balance between heat production and thermal exchange, an increase in K also leads to the acceleration of the combustion front [56]. As a conclusion, further investigations should be necessary to determine the effect of mechanical pretreatment on thermal exchange during combustion.

CONCLUSION

MASHS process is a suitable technique to produce nanocrystalline molybdenum disilicide. To prevent the formation of parasite phases, the control of all the parameters during ball milling step such as, for example, the mechanical injected power or the amount of new phases induced by direct mechanical alloying is essential in the MASHS process. In order to obtain nanostructured intermetallic α-MoSi$_2$, it is important to prepare nano-structured mixture between Mo (50 nm) and Si (30 nm) crystallites with very good contacts inside a micrometric powder particle.

Mechanical activation can multiply the combustion front velocity by a factor of three (up to 42 mm/s) compared to classical value obtained under the same ignition conditions. In addition, high-energy ball milling treatment allows to control the formation of a pure and nanometric α-MoSi$_2$ (D_{MoSi_2} = 88 nm) compound by fixing the reactant powder microstructure. An increase in the contact surface between reactants at nanometric scale can improve the self-sustaining reaction compared with classical SHS process. But some complementary *in situ* studies will be necessary to confirm the implications of mechanical alloying in microstructure development or thermal exchange during the combustion process.

REFERENCES

1 T. Kham, S. Saka, P. Veyssiere, P. Costa, Intermetallics for Structural Applications, High Temperature Materials for Power Engineering 1990 Liege, Sept. 24−27, 1990.

2 M. J. Maloney, D. Shah, Advanced Intermetallics − Silicide, Physical Metallurgy and Processing of Intermetallic Compounds, in N. B. Stoloff and V. K. Sikka (Eds.), Thomson Publ., p. 441.

3 Y. Jeng, B. J. Lavernia, *J. Mater. Sci.*, 29 (1994) 2557.

4 N. S. Stoloff, *Mater. Sci. Eng. A*, A261 (1999) 169.

5 T. B. Massalski, Mo−Si Equilibrium Phase Diagram, in: Binary Alloy Phase Diagrams, 2 (1990) 2666.

6 S. Zhang and Z. A. Munir, *J. Mater. Sci.*, 26 (1991) 3685.

7 G. Le Caër, E. Bauer-Grosse, A. Pianelly *et al.*, *Ibid.*, 25 (1990) 4726.

8 R. B. Schwartz, S. R. Srinivasan, J. J. Petrovic, S. J. Maggiore, *Mater. Sci. Eng. A*, A115 (1992) 75.

9 S. N. Patankar, S. Q. Xiao, J. J. Lewandowski, A. H. Heuer, *J. Mater. Res.*, 8, 6 (1993) 1311.

10 B. K. Yen, T. Aizawa, J. Kihara, *Mater. Sci. Forum*, 225–227 (1996) 252.

11 A. G. Merzhanov, I. P. Borovinskaya, *DAN SSSR*, 204 (1972) 366.

12 J. M. Lihrman, J. L. Chermant, *Ann. Chim. Fr.*, 20 (1995) 93.

13 Z. A. Munir, *Ceram. Bull.*, 2 (1988) 342.

14 J. J. Moore, H. J. Feng, *Prog. Mater. Sci.*, 39 (1995) 272.

15 E. Gaffet, N. Malhouroux-Gaffet, *J. All. Comp.*, 205 (1994) 27.

16 N. Malhouroux-Gaffet, E. Gaffet, *Ibid.*, 198 (1993) 143.

17 F. Charlot, E. Gaffet, F. Bernard *et al.*, *Mater. Sci. Forum*, 269–272 (1998) 379.

18 V. Gauthier, C. Josse, F. Bernard *et al.*, *Mater. Sci. Eng. A*, A265 (1999) 117.

19 V. Gauthier, F. Bernard, E. Gaffet *et al.*, *Ibid.*, A272 (1999) 334.

20 F. Charlot, E. Gaffet, B. Zeghmati *et al.*, *Ibid.*, A262 (1999) 279.

21 F. Charlot, E. Gaffet, F. Bernard, J. C. Niepce, *Acta Mater.*, 47 (1998) 619.

22 F. Charlot, E. Gaffet, F. Bernard *et al.*, *Mater. Sci. Forum*, 312–314 (1999) 287.

23 M. Abdellaoui, E. Gaffet, *J. All. Comp.*, 198 (1993) 155.

24 M. Abdellaoui, E. Gaffet, *Acta Mater.*, 44 (1996) 725.

25 E. Gaffet, N. Malhouroux, M. Abdellaoui, *J. All Comp.*, 194 (1993) 339.

26 S. Brunauer, P. Emmett, E. Teller, *J. Amer. Chem. Soc.*, 60 (1938) 309.

27 J. F. Javel, M. Dirand, J. J. Kuntz *et al.*, *J. All. Comp.*, 247 (1997) 72.

28 Private Communication F. Papini IUSTI-CNRS, Marseille, France.

29 R. Sandaresan, F. H. Froes, *J. Metals*, Aug. (1987) 22.

30 E. Gaffet, O. Tillement, *Ann. Chim. Sci. Mat.*, 22 (1997) 412.

31 B. B. Bokhonov, I. G. Konstanchuk, V. V. Boldyrev, *J. All. Comp.*, 218 (1995) 190.

32 S. Liu, X. Qu, Z. Liu, B. Huang, *J. Mater. Sci. Technol.*, 15 (1999) 423.

33 C. Halder, C. N. J. Wagner, *Acta Cryst.*, 20 (1996) 312.

34 J. Plevert, D. Louer, *J. Chim. Phys.*, 87 (1990) 1427.

35 J. Plevert, PhD Thesis, University of Rennes, France, 1980.

36 J. L. Langford, Proc. of Int. Conf. Accurancy in Powder Diffraction II, held at NIST, Gaitherburg, MD, May 26–29, 1992.

37 Z. A. Munir, *J. Mat. Synth. Proc.*, 1 (1993) 387.

38 R. W. Rice, W. J. McDonnough, *J. Am. Ceram. Soc.*, 68 (1985) C122.

39 G. B. Schaffer, P. G. McCormick, *Mater. Sci. Forum*, 16 (1992) 91.

40 E. Gaffet, F. Bernard, J. C. Niepce *et al.*, *J. Mater. Chem.*, 9 (1999) 305.

41 H. P. Li, *J. Chin. I. Ch. E.*, 22, 1 (1999) 1.

42 J. Lagerbom, T. Tiainen, M. Lehtonen, P. Lintula, *J. Mater. Sci.*, 34 (1999) 1477.

43 T. S. Dyer, Z. A. Munir, *Metal. Mater. Trans. B*, 26B (1995) 603.

44 M. R. Reiss, C. M. Esber, D. Van Heerden *et al.*, *Mater. Sci. Eng. A*, A261 (1999) 217.

45 Ch. Cras, F. Charlot, E. Gaffet *et al.*, *Acta Mater.*, 47, 7 (1999) 2113.

46 Ch. Gras, E. Gaffet, F. Bernard *et al.*, *Mater. Sci. Forum*, 312–314 (1999) 281.

47 S. C. Deevi, *J. Mat. Sci.*, 26 (1991) 3343.

48 S. C. Deevi, *Mat. Sci. Eng.*, A419 (1992) 241.

49 Sung-Wang Jo, Gi-Wook Lee, Jong-Tae Moon, Yong-Seog Kim, *Acta Mater.*, 24, 11 (1996) 4317.

50 A. G. Merzhanov, I. P. Borovinskaya, I. O. Khomeko *et al.*, *Ann. Chim. Fr.*, 20 (1995) 123.

51 P. Zhu, J. C. M. Li, C. T. Liu, *Mater. Sci. Eng. A.*, A239–240 (1997) 532.

52 F. Bordeaux, A. R. Yavari, P. Desre, *Review Phys. Appl.*, 22 (1997) 107.

53 A. Makino, C. K. Law, *J. Am. Ceram. Soc.*, 79, 12 (1996) 3097.

54 L. L. Wang, Z. A. Munir, *Met Mat. Trans. B*, June 26B (1995) 595.

55 Y. Zhang, G. C. Stangle, *J. Mater. Res.*, 10, 4 (1995) 1962.

56 E. M. Carillo-Heian, O. A. Graeve, A. Feng *et al.*, *J. Mater. Res.*, 14, 5 (1999) 1949.